



# Revealing the interplay between “intelligent behavior” and surface reconstruction of non-precious metal doped SrTiO<sub>3</sub> catalysts during methane combustion<sup>☆</sup>

Zhenghong Bao <sup>a</sup>, Victor Fung <sup>b</sup>, Jisue Moon <sup>a</sup>, Zachary D. Hood <sup>c</sup>, Maria Rochow <sup>a,d</sup>, James Kammert <sup>a</sup>, Felipe Polo-Garzon <sup>a,\*</sup>, Zili Wu <sup>a,b,\*\*</sup>

<sup>a</sup> Chemical Sciences Division, Oak Ridge National Laboratory, Oak Ridge, TN 37830, United States

<sup>b</sup> Center for Nanophase Materials, Oak Ridge National Laboratory, Oak Ridge, TN 37830, United States

<sup>c</sup> Applied Materials Division, Argonne National Laboratory, Lemont, IL 60439, United States

<sup>d</sup> Department of Materials Science and Engineering, Michigan Technological University, Houghton, MI 49931, United States

## ARTICLE INFO

### Keywords:

“intelligent behavior”  
Surface reconstruction  
Methane combustion  
Doped perovskites

## ABSTRACT

The impact of surface reconstruction of a model perovskite, SrTiO<sub>3</sub> (STO), on CH<sub>4</sub> activation for combustion and oxidative coupling was previously revealed that the reaction rate was proportional to the creation of Sr-terminated step sites. Doped perovskites (SrTi<sub>1-x</sub>M<sub>x</sub>O<sub>3</sub>, M=metal dopant) present yet another form of reconstruction throughout the surface and the bulk, where the metal dopant can migrate in and out of the perovskite lattice, also known as “intelligent behavior”. In this work, understanding the interplay between perovskite surface reconstruction (surface termination) and the “intelligent behavior” is tackled for the first time, and the catalytic consequences are probed with CH<sub>4</sub> combustion as a model reaction. A set of experimental techniques, including XRD, Raman spectroscopy, X-ray adsorption spectroscopy, kinetic measurements, as well as DFT calculations were used to understand the catalytic behavior of the reconstructed surfaces of Ni and Cu-doped STO for methane combustion. We found that during methane oxidation, the diffusion of Ni and Cu into the lattice due to the “intelligent behavior” is accompanied by Sr enrichment on the surface of the perovskite. This Sr-enrichment process is reversible when Cu or Ni species exsolute as clusters/nanoparticles upon H<sub>2</sub> treatment. Such a surface reconstruction is found to greatly impact the catalytic activity of doped perovskites towards methane combustion.

## 1. Introduction

Catalytic combustion of methane has received renewed attention in the past decades for various applications in pollution abatement and thermal energy production, due to the increase in production of shale gas [1,2]. Catalytic combustion of methane is viewed as a more efficient, environmentally benign alternative to the conventional flaring for energy production, as it reduces operation temperatures and emissions of noxious and greenhouse gases. In particular, unburned methane

released during incomplete thermal combustion poses a serious environmental problem, as methane is a gas with a greenhouse effect 20-times stronger than that of CO<sub>2</sub> [3,4].

The most well-known methane combustion catalyst is Pd, but the cost and catalyst stability have fueled interest in alternative, inexpensive catalysts such as perovskite oxides. Perovskite oxides have a general formula of ABO<sub>3</sub>, where A is an alkali, alkaline or rare-earth cation, and B is a transition metal cation. Perovskites have been extensively studied in thermal catalysis, electrocatalysis and photocatalysis because of their

<sup>☆</sup> Notice: This manuscript has been authored by UT-Battelle, LLC under Contract No. DE-AC05-00OR22725 with the U.S. Department of Energy. The United States Government retains and the publisher, by accepting the article for publication, acknowledges that the United States Government retains a non-exclusive, paid-up, irrevocable, world-wide license to publish or reproduce the published form of this manuscript, or allow others to do so, for United States Government purposes. The Department of Energy will provide public access to these results of federally sponsored research in accordance with the DOE Public Access Plan (<http://energy.gov/downloads/doe-public-access-plan>)

\* Corresponding author.

\*\* Corresponding author at: Chemical Sciences Division, Oak Ridge National Laboratory, Oak Ridge, TN 37830, United States.

E-mail addresses: [pologarzon@ornl.gov](mailto:pologarzon@ornl.gov) (F. Polo-Garzon), [wuz1@ornl.gov](mailto:wuz1@ornl.gov) (Z. Wu).

<https://doi.org/10.1016/j.cattod.2022.03.012>

Received 9 December 2021; Received in revised form 5 February 2022; Accepted 14 March 2022

Available online 19 March 2022

0920-5861/© 2022 Elsevier B.V. All rights reserved.

tunability in composition and structure. The surface termination of perovskites can greatly differ from the stoichiometric composition, and different surface terminations can lead to different catalytic performance [5]. Recently, Polo-Garzon et al. reported that rates for methane combustion over  $\text{SrTiO}_3$  (STO) catalysts can vary up to 1 order of magnitude, depending on the surface reconstruction, and it was found that Sr-terminated step-sites favored  $\text{CH}_4$  activation [6].

Although perovskite catalysts have a high thermal stability, their activities in methane combustion are still low compared to precious metal-based catalysts. Therefore, modification of perovskites with doped and supported metals has been generally adopted to improve the catalytic activity [7–9]. A precious-metal doped perovskite can function as an “intelligent” catalyst that generates metallic nanoparticles and release oxygen from the perovskite oxide under reducing conditions and reabsorb the precious metal and oxygen into the perovskite oxide in oxidative environment at elevated temperatures [10,11]. Although such an “intelligent behavior” has been demonstrated extensively for perovskite-supported noble metals, it has been rarely shown that transition metals, such as Cu and Ni that are active for methane activation, can also provide such a behavior [12,13]. Furthermore, we expect the “intelligent behavior” to coexist with changes in the surface termination/reconstruction of the host perovskite. However, the interplay between the surface reconstruction of perovskites and the “intelligent behavior” remains largely unexplored since the impact of surface reconstruction of perovskites for heterogeneous catalysis was only recently recognized [5,14]. This fundamental knowledge is crucial to design catalytic surfaces with optimal structures for the activation of reactants. In this work,  $\text{CH}_4$  combustion over Ni and Cu-doped STO has been chosen as the model systems to unveil the impact of catalyst reconstruction and “intelligent behavior” of doped perovskites on methane activation and conversion. Relatively high doping levels, 3–10 mol% mostly reported in literature, were widely adopted to impact the performance of pristine perovskites [15,16]. Here, 10 mol% of Ti in  $\text{SrTiO}_3$  was intended to be substituted by Ni and Cu for an enhanced catalytic performance in methane activation.

## 2. Experimental methods

### 2.1. Catalyst synthesis

Metal doped STO nanocubes (Ni-STO, Cu-STO) were prepared by modified hydrothermal synthesis [14]. In detail, an ice bath using a 500-mL glass trough was firstly set up on a magnetic stirring stage. 14.5 mL DI water was added into a 150-mL beaker located in the ice bath. 227  $\mu\text{L}$  titanium chloride ( $\text{TiCl}_4$ , 99.9%, Sigma-Aldrich) were added dropwise into the beaker under a stirring of 400 rpm for 5 min, then 0.066 mg  $\text{Ni}(\text{NO}_3)_2 \cdot 6\text{H}_2\text{O}$  (99%, Sigma-Aldrich) or 0.055 mg  $\text{Cu}(\text{NO}_3)_2 \cdot 3\text{H}_2\text{O}$  (99%, Sigma-Aldrich) were added. Thereafter 28.5 mL 3 M  $\text{LiOH} \cdot \text{H}_2\text{O}$  (>98% SigmaAldrich) were added followed by a stirring for 30 min. Next, 9.5 mL 0.24 M  $\text{SrCl}_2 \cdot 6\text{H}_2\text{O}$  (>99%, Alfa Aesar) were added, followed by stirring for another 30 min. The resultant mixtures were transferred into 45 mL-Teflon autoclaves (Parr 5000 Multi Reactor Stirrer System), heated to 180 °C and held for 48 h at a stirring rate of 800 rpm. After cooling to room temperature, the samples were centrifuged at 10000 rpm for 10 min. The collected samples were washed five times in deionized water and three times in ethanol. After drying the samples in a vacuum oven at 70 °C for 12 h, they were calcined in air at 550 °C for 4 h, which are denoted as Ni-STO ( $\text{SrTi}_{0.9}\text{Ni}_{0.1}\text{O}_3$ ) and Cu-STO ( $\text{SrTi}_{0.9}\text{Cu}_{0.1}\text{O}_3$ ) respectively. The pristine  $\text{SrTiO}_3$  was prepared using a similar procedure without adding neither Ni nor Cu precursors. In addition, catalysts of nickel and copper supported STO (NiO/STO, CuO/STO) were prepared by incipient wetness impregnation method with 10 mol% metal loading.

### 2.2. Catalyst evaluation

The catalytic activities for methane combustion over metal doped STO were evaluated on AMI-200. Each catalyst (0.100 g, 60–80 mesh) was loaded inside a quartz U-tube and held in place by placing quartz wool at both ends of the bed. The pretreated sample was performed under 30 mL/min of 5%  $\text{O}_2/\text{Ar}$  at 800 °C for 5 h ( $\text{O}_2$  treatment) or under 30 mL/min of 4%  $\text{H}_2/\text{Ar}$  at 800 °C for 2 h ( $\text{H}_2$  treatment) and then cooled to 50 °C. Subsequently, a feed gas of 6 mL/min 5%  $\text{O}_2/\text{Ar}$  and 5 mL/min 1%  $\text{CH}_4/\text{Ar}$  was introduced into the reactor. Reaction temperature was ramped up to 800 °C at 2 °C/min. Products were analyzed using a Buck Scientific Model 910 gas chromatograph (GC) equipped with a flame ionization detector and a ShinCarbon ST column.

### 2.3. Characterizations

**Powder X-ray diffraction** (XRD) patterns were obtained using a PANalytical X'Pert Pro MPD diffractometer with  $\text{Cu K}\alpha$  radiation ( $\lambda = 1.5418 \text{ \AA}$ ) at the conditions of 44 kV, 40 mA, and  $2\theta = 10 - 90^\circ$ . The step size for each measurement was 0.0167°. Rietveld refinement of the crystal structures obtained from XRD was performed using the program GSAS-II [17]. The zero point of the scale, three reflection widths (Caglioti formula, U, V, and W), the lattice parameter, the atomic site parameter and the isotropic thermal displacement parameters were allowed to vary during refinements.

**Raman spectroscopy** was performed on a multiwavelength Raman system [18] at room temperature. Raman spectral was collected with 325 nm laser excitation. Raman scattering was collected via a customized ellipsoidal mirror and directed by a fiber optics bundle to the spectrograph stage of a triple Raman spectrometer (Princeton Instruments Acton Trivista 555). Edge filters (Semrock) were used in front of the UV-vis fiber optic bundle (Princeton Instruments) to block the laser irradiation. The 325 nm (10 mW at sample) excitation laser is generated from a HeCd laser (Melles Griot). A UV-enhanced liquid  $\text{N}_2$ -cooled CCD detector (Princeton Instrument) was employed for signal detection.

**X-ray absorption spectroscopy** (XAS) were conducted in the 7-BM beamline (QAS) at National Synchrotron Light Source-II (NSLS-II) at Brookhaven National Laboratory to verify the success doping of metals into STO. The X-ray source was generated by the ring energy of 10 keV and the current of 400 mA, and was mono-chromatized by a Si (111) double crystal monochromator before it reaching the samples with a spot size of ~300  $\mu\text{m}$ . Cu-K, Ni-K, Sr-K X-ray absorption near edge spectroscopy (XANES) data for samples with various treatments (as-synthesized,  $\text{O}_2$  treatment,  $\text{H}_2$  treatment and 2nd  $\text{O}_2$  treatment) were collected in transmission mode along with standards for further calibrating the edge energy ( $E_0$ ) of the sample under measurement.

**X-ray photoelectron spectroscopy** (XPS) spectra were collected for each powder sample on a Thermo K-Alpha XPS system ( $\text{Al K}\alpha$  X-ray source, 1486.6 eV) with a spot size of 400  $\mu\text{m}$  and a resolution of 0.1 eV. Samples were etched with  $\text{Ar}^+$  sputtering at a rate of 0.1 nm/sec to perform depth profiling. All spectra were processed using Thermo Avantage, which is a software package provided through ThermoScientific.

**Temperature programmed oxygen isotopic exchange** (TPOIE) was performed on an Altamira Instruments system (AMI-200). 30 mg catalyst was loaded and pretreated in regular oxygen at 550 °C for 1 h, later, the temperature was decreased to 40 °C. A gas flow of 30 mL/min 1%  $^{18}\text{O}_2/\text{He}$  was introduced in the system for 10 min, and then the temperature was ramped up (10 °C/min) to 850 °C and kept for 40 min. During this increase in temperature,  $^{18}\text{O}_2$  in gas phase will exchange with the oxygen in the catalyst lattice. MS signals were recorded at  $m/z$  of 32, 34 and 36, representing  $^{16}\text{O}_2$ ,  $^{16}\text{O}^{18}\text{O}$  and  $^{18}\text{O}_2$ , respectively.

## 2.4. DFT calculations

Density functional theory calculations (DFT) were performed with the Vienna Ab Initio Simulation Package (VASP) [19,20]. The Perdew-Burke-Ernzerhof (PBE)[21] functional within the generalized-gradient approximation (GGA) was used for electron exchange and correlation energies. Dispersion corrections were added using the D3 method by Grimme [22]. The projector-augmented wave method was used to describe the electron-core interaction [19,23]. A kinetic energy cutoff of 450 eV was used. All calculations were performed with spin polarization. The Brillouin zone was sampled using a Monkhorst-Pack scheme with a  $2 \times 2 \times 1$  grid [24]. A vacuum layer of 15 Å was used for the surface slabs along the z-direction and the atoms in the bottom two layers were fixed during the calculations. Surfaces were modelled with a  $2 \times 2$  supercell of the (100) facet slab. Transition states (TS) were found with the nudged elastic band (NEB) [25] method with a force convergence criterion of 0.05 eV/Å.

## 3. Results and discussion

### 3.1. Structural properties of the catalysts

Pristine STO synthesized by the hydrothermal method is of a cubic shape with exposed surfaces composed primarily of the (100) facet [14]. Ni and Cu-doped STO nanocubes ( $\text{SrTi}_{0.9}\text{Ni}_{0.1}\text{O}_3$  and  $\text{SrTi}_{0.9}\text{Cu}_{0.1}\text{O}_3$ , respectively) were prepared via the similar method to incorporate Ni and Cu ions into the lattice of STO. SEM images show that Ni-STO and Cu-STO with nanocube morphology were successfully synthesized (Fig. S1). X-ray diffraction patterns of the as-synthesized Cu and Ni-doped STO samples showed similar diffraction pattern to that of the undoped STO (Fig. S2A). The highest intensity diffraction peak of STO, related to the (110) plane (~32.4°), shifts to lower angles when STO is doped (Fig. S2B). Lower diffraction angles result in smaller lattice parameters based on the Bragg's law, indicating the creation of oxygen vacancies to compensate charge deficiency when the  $\text{M}^{2+}$  substitutes  $\text{Ti}^{4+}$  [26]. This suggests, along with the absence of any peaks corresponding to metallic or oxidized Cu or Ni, that Ni and Cu were successfully doped into the STO lattice.

To elucidate whether Ni and Cu were doped either in the A or in the B position of the perovskite ( $\text{ABO}_3$ ), we performed Rietveld refinement of the XRD patterns (Fig. S2A). The corresponding refinements of pristine STO and metal doped STO catalysts exhibited a good fit between the models and experimental observations. The models for the metal doped samples are based on the substitution of the Ti-cation rather than the Sr-cation. Therefore, we concluded that Ni and Cu most likely reside in the B-position of the perovskite. The pristine STO matches well with Pm3m space group, while the metal doped samples belong to the I4/mcm group. This is consistent with previous reports, where a  $\text{SrTi}_y\text{Zr}_{1-y}\text{O}_3$  system has a cubic Pm3m structure when  $0.95 < y \leq 1$ , a tetragonal I4/mcm structure when  $0.4 < y \leq 0.95$ , and an orthorhombic Pbnn structure when  $0 \leq y \leq 0.4$  [27]. The parameters of the structure refinements are listed in Table S1. For the samples with further O<sub>2</sub> or H<sub>2</sub> treatment (Fig. S2B), no diffraction peaks were ascribed to the oxides of Cu and Ni or metallic Cu and Ni. Even though, XRD measurements did not reveal crystal phases other than the perovskite, small clusters of Cu or Ni may be undetectable by XRD.

Raman spectroscopy was attempted to identify secondary crystallographic phases on the Ni-STO and Cu-STO samples after treatment at 550 °C in H<sub>2</sub> or O<sub>2</sub> (Fig. S3). Treatment at 550 °C in O<sub>2</sub> has been reported to reconstruct the surface for pure  $\text{SrTiO}_3$ ,  $\text{SrZrO}_3$ ,  $\text{BaTiO}_3$ , and  $\text{BaZrO}_3$  perovskites [14,28,29]. Therefore, we have chosen these treatment conditions to evaluate the reconstruction of our catalysts. The Raman spectroscopy results show the same peak positions in all metal doped samples as those of the pristine STO, but the peak intensities of the metal doped samples were lower (Fig. S3). Table S2 summarizes the relative intensity (normalization of the integrated peak area) of the

high-frequency scattering feature at 1600 cm<sup>-1</sup> for all samples, as well as the peak assignments for all peaks. The absence of a vibrational mode at 600 cm<sup>-1</sup> suggests there is no CuO phase in the Cu-STO sample [30, 31]. The absence of peaks at 1100 cm<sup>-1</sup> and 1500 cm<sup>-1</sup> indicates the absence of a bulk NiO phase in the Ni-STO sample [32]. In addition, the absence of vibrational modes near 1075 cm<sup>-1</sup> indicate  $\text{SrCO}_3$  is not present in any of the samples studied [33].

Ex situ XAS characterization at the Ni, Cu K-edge was carried out for the Ni, Cu-doped STO samples with different treatments to understand oxidation state and coordination number of the dopants, Ni and Cu, in the lattice. The XANES data for as-synthesized, O<sub>2</sub> treated, H<sub>2</sub> treated and 2nd O<sub>2</sub> treated samples, together with the reference data for Ni, Cu foils, NiO and CuO, are presented in Fig. 1. Evaluation of as-synthesized and O<sub>2</sub> treated samples clearly demonstrates a nonmetallic state of Ni and Cu. In contrast to as-synthesized and O<sub>2</sub> treated sample data, results for samples subjected to H<sub>2</sub> treatment indicate that all reduced samples contained a fraction of metallic Ni or Cu. The molar fractions of each phase were obtained using a linear combination fitting analysis, revealing that about 75.5% of the Ni atoms were in the metallic Ni phase (likely in nanoparticle form) for H<sub>2</sub> treated Ni-STO, and about 77.2% the Cu atoms were in the metallic Cu phase (likely in nanoparticle form) for H<sub>2</sub> treated Cu-STO. The EXAFS analysis was applied to determine the local structure of Ni and Cu atoms in each phase. The experimental EXAFS data and results from fitting the data with theoretical models (B site partially substituted by Ni or Cu) for as synthesized samples are shown in Fig. S4, and the estimated local structure parameters are given in Table S3. The good agreement between this model and the experimental results suggests that Cu and Ni are incorporated into the lattice of STO. In contrast, Ni is not expected to be incorporated into the A sites of strontium titanate. The low stability of Ni at the A site of  $\text{SrTiO}_3$  may be related to the large difference in the ionic radii of  $\text{Ni}^{2+}$  (0.69 Å) is much less than that of  $\text{Sr}^{2+}$  (1.18 Å) [34]. Copper was reported to occupy the Ti octahedral sites in either Sr or Ti over stoichiometric STO ceramics with nominal compositions of  $\text{SrTi}_{1-x}\text{O}_3:\text{xCuO}$  ( $0.002 \leq x \leq 0.1$ ) or  $\text{Sr}_{1-x}\text{TiO}_3:\text{xCuO}$  ( $0.01 \leq x \leq 0.2$ ) [26].

### 3.2. Surface composition of the doped STOs

Bulk phase results from XRD, Rietveld refinement, Raman measurements and EXAFS analysis suggest that the Cu and Ni have been doped into the lattice of STO and under O<sub>2</sub>-treatment condition. To characterize the surface of the samples, X-ray photoelectron spectroscopy (XPS) with depth profiling (Fig. S5) was employed to reveal the surface composition. It is worth to point out that the XPS probing depth is a few nm, while the sputtering depth is 0.3 nm each step, which means the XPS data always represent the average surface composition of top a few nm along with the surface sputtering. The elemental surface composition of Ni-STO and Cu-STO at zero sputtering depth are shown in Fig. 2.

The as-synthesized samples have a slight Ni or Cu enrichment at the surface compared with the bulk ( $\text{Ni}/(\text{Ni}+\text{Ti}+\text{Sr}) = 0.05$ ), a slight Ti deficiency compared with the bulk, and a stable Sr distribution along with the probing depth (Fig. S5), indicating that more Ti cations were substituted by Ni or Cu at the surface compared to the bulk. This is reasonable because the as-synthesized pristine STO is Ti-enriched at the surface [6,14,29] and thus allows substitution by Ni or Cu. Even though the as-synthesized samples are surface-enriched with the dopant, the dopant is not expected to be in the metallic state, according to XAS results (Fig. 1); therefore, we can conclude the surface of the as-synthesized samples is enriched with Ni or Cu cations.

After O<sub>2</sub> treatment, the concentration of Ni or Cu significantly reduced on the surface (2–4%) compared to that of the as-synthesized samples (~10%), meanwhile, Ti concentration remained approximately the same, and the concentration of Sr increased. Thus, upon O<sub>2</sub>

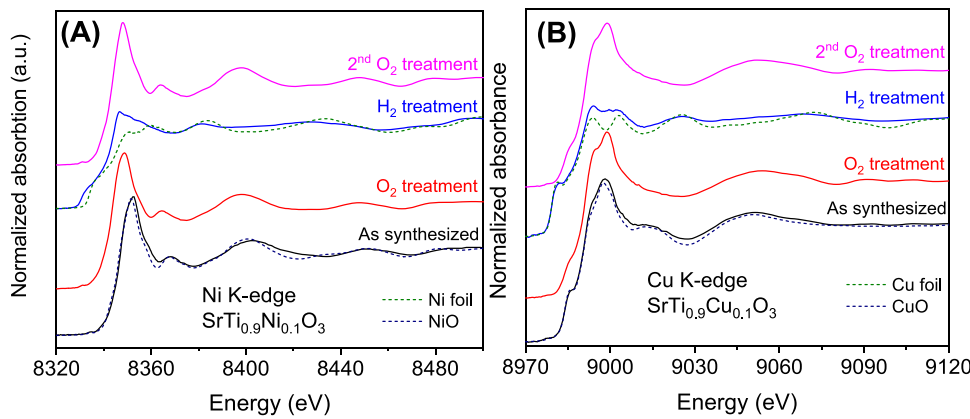


**Fig. 1.** Fourier transform magnitudes of  $k^2$ -weighted XANES spectra of (A) Ni and (B) Cu doped STO perovskite. As-synthesized: stored at ambient for an extended period (weeks) with no further treatment after the sample synthesis with air treatment at 550 °C for 5 h; O<sub>2</sub> treatment and 2nd O<sub>2</sub> treatment: annealed in 5% O<sub>2</sub>/Ar at 800 °C for 5 h before the XAS measurement; H<sub>2</sub> treatment: heated in 4% H<sub>2</sub>/Ar at 800 °C for 2 h before the XAS measurement.

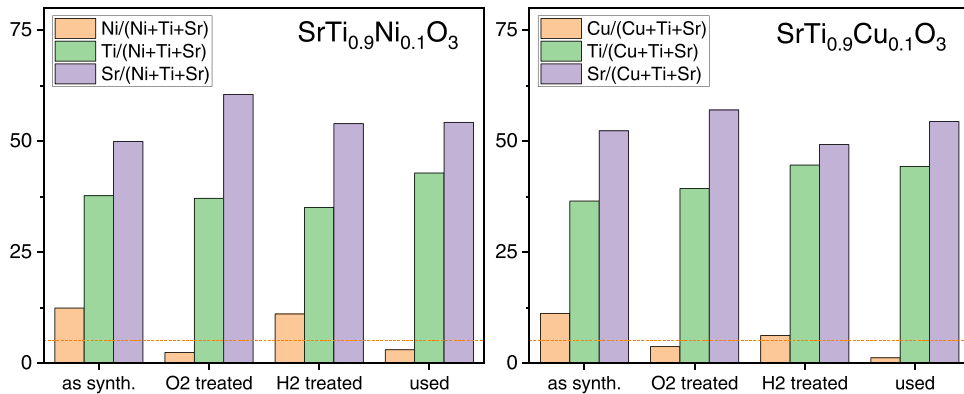


**Fig. 2.** The elements composition of the top probing layer in XPS depth profile on Ni and Cu doped STO samples after different treatments. The dashed lines represent the theoretical bulk compositions of dopants (5%, M/(M+Ti+Sr)=0.05). As-synthesized: no further treatment after the sample synthesis with air treatment at 550 °C for 5 h; O<sub>2</sub> treatment: annealed in 5% O<sub>2</sub>/Ar at 800 °C for 5 h before the XPS measurement; H<sub>2</sub> treatment: heated in 4% H<sub>2</sub>/Ar at 800 °C for 2 h before the XPS measurement. Used samples came from the as synthesized samples after catalytic combustion of methane from RT to 800 °C at 2 °C/min.

treatment, Ni and Cu diffused into the bulk of the STO lattice, whereas the STO surface became enriched with Sr.

Upon H<sub>2</sub> treatment after the O<sub>2</sub> treatment, Ni and Cu segregated at the STO surface (Fig. 2), while Sr appeared to diffuse back into the lattice. This segregation is in the form of clusters/nanoparticles per XANES results (Fig. 1). These results show the “intelligent behavior” of Ni-STO and Cu-STO, where Ni and Cu diffuse into the lattice upon O<sub>2</sub> treatment, and exsolute upon H<sub>2</sub> treatment. Further, we show for the first time that this dynamic behavior of the dopant correlates with changes in the surface termination of the host perovskite, where diffusion of the dopant into the lattice B sites occurs in tandem with segregation of A-site Sr at the surface. This segregation of Sr is reversible when Cu or Ni exsolute as clusters/nanoparticles upon H<sub>2</sub> treatment.

The used samples, after catalytic methane oxidation test over the as synthesized samples, showed a similar surface composition trend with that of the O<sub>2</sub> treated samples, as might be expected because the catalytic combustion of methane was operated under highly oxidizing conditions (O<sub>2</sub>/CH<sub>4</sub>=6).

When the sputtering depth was increased to 4 nm, the concentration of Ni for the as-synthesized, O<sub>2</sub> treated, H<sub>2</sub> treated, and used Ni-STO samples were 8.3%, 7.6%, 5.9% and 4.6%, respectively, and the concentration of Cu for the as-synthesized, O<sub>2</sub> treated, H<sub>2</sub> treated, and used Cu-STO samples were 7.1%, 8.0%, 3.3% and 3.2%, sequentially, which approximated the stoichiometric value, 5% (Fig. S5).

### 3.3. Methane combustion reactivity

The implications of the segregation of Sr at the surface of STO and the “intelligent behavior” of the dopants for catalysis were evaluated.

Ni-STO, Cu-STO and STO were tested for catalytic combustion of methane in a temperature-programmed surface reaction (TPSR) experiment, going from room temperature to 800 °C with a ramping rate of 2 °C/min (Fig. 3A-B). For both Ni and Cu doped STO, the as-synthesized samples (Cu and Ni enriched at the surface as cations, not as metallic clusters/nanoparticles according to XAS results in Fig. 1) showed activity at moderate temperature (starting at ~400 °C and ~450 °C for Ni-STO and Cu-STO, respectively). For Ni-STO (Fig. 3A), the activity decayed after the reaction temperature reaches 600 °C, presumably because Ni diffuses into the lattice under the oxidizing environment of the reaction. Cu-STO was less active than Ni-STO at moderate temperatures (~600 °C). The reaction rate over the as-synthesized Cu-STO increased monotonically with reaction temperature. To corroborate that the activity decrease of the as-synthesized Ni-STO at reaction temperatures above 600 °C is due to diffusion of Ni into the lattice under the oxidizing environment of the reaction, the sample was treated in O<sub>2</sub> at 800 °C before the TPSR procedure. Indeed, the activity below moderate temperature (~600 °C) was negligible because Ni was not exposed at the surface. For the case of Cu-STO (Fig. 3B), the O<sub>2</sub> treatment at 800 °C also resulted in slightly lower reaction rates in methane oxidation compared with the as-synthesized sample.

H<sub>2</sub> treatment of Ni-STO and Cu-STO resulted in low-temperature activity (starting at ~400 °C) for methane oxidation, due to the formation of metallic clusters on the surface. For Ni-STO, the as-synthesized and H<sub>2</sub>-treated samples have similar concentration of Ni, Sr and Ti at the surface, thus the difference in catalytic activity stems from the fact that Ni or NiO<sub>x</sub> nanoparticles (metallic Ni NPs start to oxidize at ~300 °C [35]) are more active than the lattice cationic Ni species. For the Cu-STO sample, H<sub>2</sub>-treatment induced high Ti content at

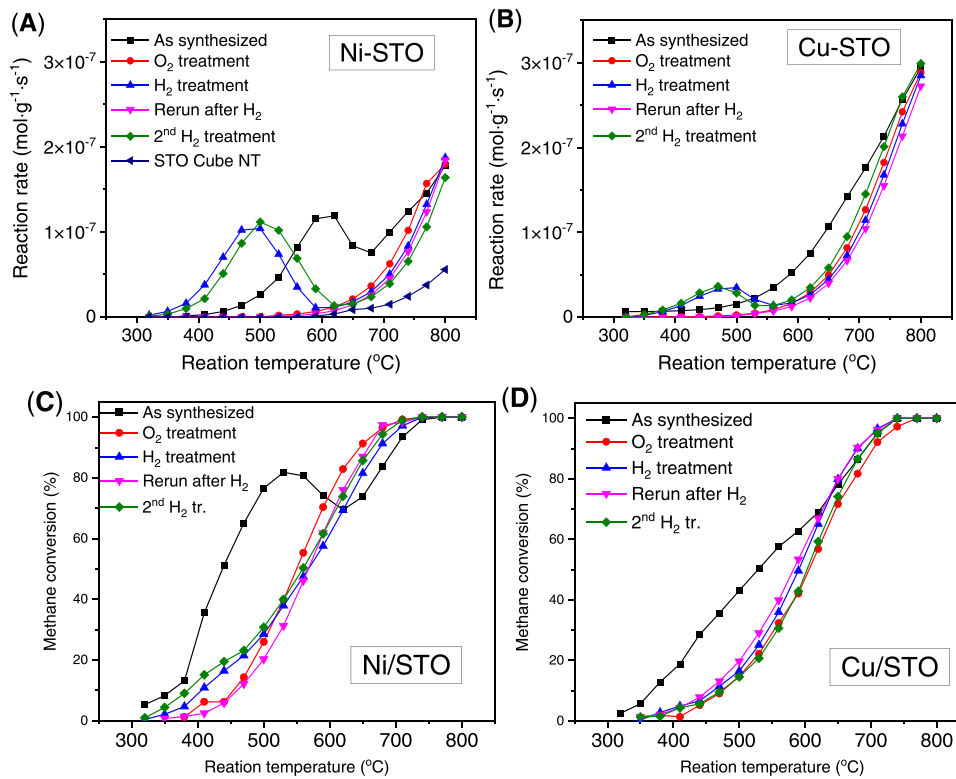


**Fig. 3.** Methane combustion over (A) Ni-doped  $\text{SrTiO}_3$ ; Ni-STO, (B) Cu-doped  $\text{SrTiO}_3$ ; Cu-STO, (C) Ni supported on  $\text{SrTiO}_3$ ; Ni/STO, and (D) Cu supported on  $\text{SrTiO}_3$ ; Cu/STO. Reaction condition: Catalyst loading 100 mg,  $\text{O}_2/\text{CH}_4$  ratio = 6/1, 5%  $\text{O}_2/\text{Ar}$  6 mL/min, 1%  $\text{CH}_4/\text{Ar}$  5 mL/min; As synthesized: no further treatment before conducting catalytic combustion of methane;  $\text{O}_2$  treatment: at 800 °C for 5 h, and  $\text{H}_2$  treatment: at 800 °C for 2 h.

the surface, compared with the as-synthesized sample. For both Ni-STO and Cu-STO catalysts, the low temperature activity of the samples after  $\text{H}_2$ -treatment decayed (when reaction temperature exceeds  $\sim 475$  °C) due to the incorporation of Ni and Cu into the lattice. Incorporation of Ni and Cu into the lattice occurs at  $\sim 500$  °C due to the oxidizing environment of the reaction (feed gas  $\text{O}_2/\text{CH}_4 = 6$ ). Such an inclusion is permanent under methane oxidation condition (data labelled “Rerun after  $\text{H}_2$ ” in Fig. 3) unless another  $\text{H}_2$ -treatment to exsolute Ni and Cu is performed again (data labelled “2nd  $\text{H}_2$  treatment” in Fig. 3).

From our previous work [14,28],  $\text{O}_2$  treatment at elevated temperatures causes a change in surface termination of STO from Ti-termination to Sr-termination. In Ni-STO and Cu-STO, some Ti-cations are substituted by Ni or Cu ions, and thus, upon  $\text{O}_2$  treatment, Ni and Cu (just like Ti) are dragged into the subsurface. Since Ni and Cu occupy B-site positions inside the lattice, we synthesized the host perovskite STO with precursors in a stoichiometric composition  $\text{Sr:Ti:O}$  1:1:3, and then the proper amount of Ni and Cu was impregnated on the surface of STO to form Ni/STO and Cu/STO. By impregnating Ni and Cu on a stoichiometric STO, we aim to frustrate Ni and Cu from diffusing into the STO lattice (there are no or very limited “vacant” B-sites) upon oxidative treatment at high temperatures, thus preventing the catalyst from deactivating in the intermediate temperature regime as the reaction temperature increases. As shown in Fig. 3C, for Ni/STO, the sample treated in  $\text{H}_2$  showed slightly higher conversion up to  $\sim 500$  °C in comparison to the  $\text{O}_2$ -treated sample. Two possible reasons can be proposed: the oxidation of metallic Ni into  $\text{NiO}_x$  at higher temperatures ( $> 500$  °C) [35,36] and partial diffusion of Ni into the bulk of STO which may still have slight concentration of B-site vacancies. From Fig. 3D, the differently pretreated Cu/STO samples showed very similar catalytic performance in methane oxidation as a function of reaction temperature. It is known that metallic Cu (after  $\text{H}_2$  treatment) can be easily oxidized to  $\text{CuO}_x$  at relatively low temperatures [37,38], which explains the similar activity for  $\text{O}_2$ - and  $\text{H}_2$ -pretreated Cu/STO samples for

methane oxidation. One can also suspect that negligible Cu diffusion into the STO bulk occurs in Cu/STO as no activity dip at intermediate temperatures. However, compared to the doped STO samples (Ni-STO and Cu-STO), Ni/STO and Cu/STO do not present a maximum in methane oxidation rate at moderate temperatures ( $\sim 500$  °C), suggesting that the diffusion of Ni and Cu into the lattice is largely frustrated for Ni/STO and Cu/STO. The maximum in conversion rate at  $\sim 525$  °C for the as-synthesized Ni/STO is possibly due to surface stabilization during the TPSR experiment.

#### 3.4. Methane activation

Catalytic combustion of methane requires both methane activation and oxygen activation. The Mars-van Krevelen (MvK) mechanism is widely accepted for oxidation reactions over metal oxide catalysts at high temperature, especially over perovskites [1,39]. In this mechanism, bulk oxygen ( $\beta$ -oxygen, desorbed at high temperatures) migrates to the surface, becoming available for the oxidation of the adsorbed substrate and it is quickly replaced by oxygen coming from the gaseous phase [40]. Therefore, the reduction-oxidation (redox) properties of the catalysts are expected to be important. We evaluated the oxygen-exchange capabilities of STO, Ni-STO and Cu-STO via temperature programmed oxygen isotopic exchange (TPOIE) (Fig. 4). The samples were pretreated in  $\text{O}_2$  at 550 °C to diffuse the Cu and Ni ions into the lattice.

The results of TPOIE characterization are shown in Fig. 4. The partial pressure of  $^{18}\text{O}_2$  started to decrease (or the partial pressure of  $^{16}\text{O}_2$  and  $^{16}\text{O}^{18}\text{O}$  started to increase) at 650 °C for Ni-STO and at 530 °C for Cu-STO. The exchange of  $^{18}\text{O}_2$  reached a maximum at the upper limit of temperature studied, 850 °C. By integrating the  $^{18}\text{O}_2$  consumption curves, the normalized oxygen capacity for Ni-STO is only 35% of Cu-STO. One could hypothesize that the higher methane conversion rates of the Cu-STO samples at high temperature ( $\sim 800$  °C), compared to the Ni-STO samples (Fig. 3A-B), are due to the enhanced  $\text{O}_2$ -exchange

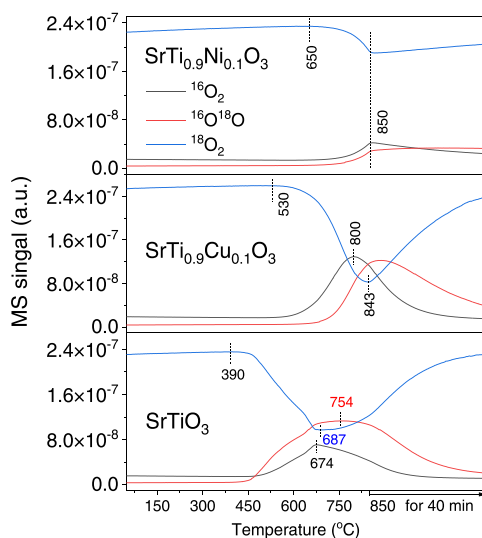


**Fig. 4.** Evolution of the oxygen isotopomers MS intensity (partial pressure) during a temperature-programmed  $^{18}\text{O}_2$  exchange on STO related catalysts. Samples pre-treat at 550 °C in  $\text{O}_2$ .

capabilities of Cu-STO; however, bare STO had even lower reaction rates compared to Ni-STO and Cu-STO, yet it had the best  $\text{O}_2$ -exchange capabilities (lower panel in Fig. 4). This experimental evidence suggests that  $\text{O}_2$ -activation is not the rate-determining step for methane oxidation under the reaction conditions studied.

Thus, we carried out some brief DFT computations to evaluate the ability of the catalysts in activating methane. The computational system chosen was a (100) terminated STO slab, which is the most abundant termination of perovskite nanocubes. The slab was terminated with Sr (according to XPS results in Fig. 2) and the metal dopant was placed in the subsurface representing the diffusion of Ni and Cu into the bulk. Ni and Cu were substituted in a B-site position (Fig. 5). We assume that the first C-H bond activation is the rate determining step [41] and thus only focused on calculating the barriers for this step. The transition state for  $\text{CH}_4$  activation over doped STO is shown in Fig. 5. The C-H activation energies were calculated to be 2.60, 1.07 and 0.55 eV for pure STO, Ni-STO and Cu-STO, respectively. This trend in activation energies qualitatively explains the trend in catalyst activity Cu-STO > Ni-STO > STO (Fig. S6) when Ni and Cu diffuse into the lattice. This confirms that first C-H bond cleavage in methane is very likely the key step in methane oxidation over the doped STO catalysts.

#### 4. Conclusions

In summary, we synthesized Ni and Cu-doped STO catalysts ( $\text{SrTi}_{0.9}\text{Ni}_{0.1}\text{O}_3$ ,  $\text{SrTi}_{0.9}\text{Cu}_{0.1}\text{O}_3$ ) and showed that the “intelligent behavior” (diffusion of Ni or Cu into the lattice as cations upon  $\text{O}_2$  treatment, and exsolution as nanoparticles upon  $\text{H}_2$  treatment) also involves segregation of Sr at the surface. Rates for methane combustion are higher when Ni or Cu are ex-solved as nanoparticles. Increasing the reaction temperature can be detrimental for reaction rates, as under the oxidizing environment of the reaction ( $\text{O}_2:\text{CH}_4 = 6:1$ ), Ni and Cu diffuse into the lattice. This reduction in reaction rates is (at least partially) suppressed in impregnated Ni(Cu)/STO samples where minimal “intelligent behavior” is present. Isotopic oxygen exchange experiments and DFT calculations suggest that  $\text{CH}_4$  activation is the rate-limiting step in the reaction mechanism of methane oxidation over the doped STO. DFT calculations show that sublayer Ni and Cu dopants favor  $\text{CH}_4$  activation on a Sr-terminated STO surface over un-doped STO, implying an indirect promotional effect of dopant on the catalytic performance of perovskites. The model system presented in this work correlates two forms of catalyst reconstruction, “intelligent behavior” and surface termination

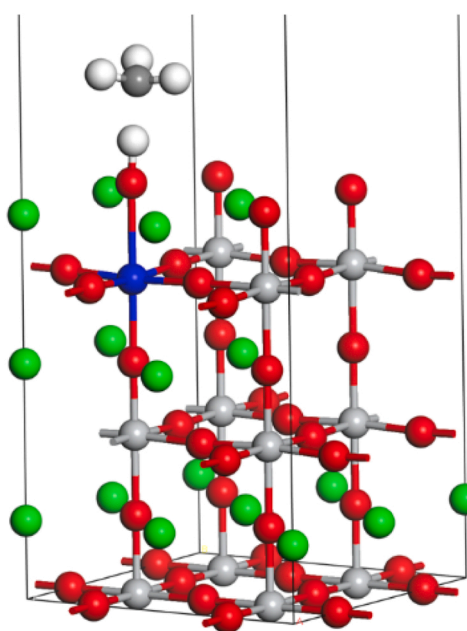


**Fig. 5.** The transition state of  $\text{CH}_4$  activation on Ni or Cu doped STO catalysts. Green: Sr, Red: O, Light grey: Ti, Dark grey: C, Blue: dopant (Cu or Ni).

of perovskites, with catalytic performance for methane combustion for the first time. Such an interplay may be further exploited to facilitate certain reactions over perovskite-based catalysts.

#### CRediT authorship contribution statement

**Zhenghong Bao:** sample preparation, data collection, writing – original draft preparation; **Victor Fung:** DFT calculations; **Jisue Moon:** X-ray absorption data; **Zachary D. Hood:** XPS data; **Maria Rochow:** catalysts synthesis; **James Kammert:** kinetic data collection; **Felipe Polo-Garzon:** data interpretation, writing – revision; **Zili Wu:** conceptualization and writing – revision.

#### Declaration of Competing Interest

The authors declare that they have no known competing financial interests or personal relationships that could have appeared to influence the work reported in this paper.

#### Acknowledgement

This research is sponsored by the U.S. Department of Energy, Office of Science, Office of Basic Energy Sciences, Chemical Sciences, Geosciences, and Biosciences Division, Catalysis Science program. Part of the work including XRD and SEM was conducted at the Center for Nanophase Materials Sciences, which is a DOE Office of Science User Facility. This research used beamline 7-BM (QAS) of the National Synchrotron Light Source II, a U.S. DOE Office of Science User Facility operated for the DOE Office of Science by Brookhaven National Laboratory under Contract No. DE-SC0012704. Beamline operations were supported in part by the Synchrotron Catalysis Consortium (U.S. DOE, Office of Basic Energy Sciences, Grant No. DE-SC0012335). This research used resources of the National Energy Research Scientific Computing Center, a DOE Office of Science User Facility supported by the Office of Science of the U.S. Department of Energy under contract no. DE-AC02-05CH11231.

## Notes

The authors declare no competing financial interest.

## Appendix A. Supporting information

Supplementary data associated with this article can be found in the online version at doi:10.1016/j.cattod.2022.03.012.

## References

- [1] J. Chen, T. Buchanan, E.A. Walker, T.J. Toops, Z. Li, P. Kunal, E.A. Kyriakidou, Mechanistic understanding of methane combustion over Ni/CeO<sub>2</sub>: a combined experimental and theoretical approach, *ACS Catal.* 11 (2021) 9345–9354.
- [2] L. Bai, F. Polo-Garzon, Z. Bao, S. Luo, B.M. Moskowitz, H. Tian, Z. Wu, Impact of surface composition of SrTiO<sub>3</sub> catalysts for oxidative coupling of methane, *ChemCatChem* 11 (2019) 2107–2117.
- [3] L.-h Xiao, K.-p Sun, X.-l Xu, X.-n Li, Low-temperature catalytic combustion of methane over Pd/CeO<sub>2</sub> prepared by deposition-precipitation method, *Catal. Commun.* 6 (2005) 796–801.
- [4] M. Carguello, J.J. Delgado Jaen, J.C. Hernandez Garrido, K. Bakhmutsky, T. Montini, J.J. Calvino Gamez, R.J. Gorte, P. Fornasiero, Exceptional activity for methane combustion over modular Pd@CeO<sub>2</sub> subunits on functionalized Al<sub>2</sub>O<sub>3</sub>, *Science* 337 (2012) 713–717.
- [5] F. Polo-Garzon, Z. Bao, X. Zhang, W. Huang, Z. Wu, Surface reconstructions of metal oxides and the consequences on catalytic chemistry, *ACS Catal.* 9 (2019) 5692–5707.
- [6] F. Polo-Garzon, V. Fung, X. Liu, Z.D. Hood, E.E. Bickel, L. Bai, H. Tian, G.S. Foo, M. Chi, D.-e Jiang, Z. Wu, Understanding the impact of surface reconstruction of perovskite catalysts on CH<sub>4</sub> activation and combustion, *ACS Catal.* 8 (2018) 10306–10315.
- [7] A. Eyssler, P. Mandaliev, A. Winkler, P. Hug, O. Safonova, R. Figi, A. Weidenkaff, D. Ferri, The effect of the state of pd on methane combustion in Pd-Doped LaFeO<sub>3</sub>, *J. Phys. Chem. C* 114 (2010) 4584–4594.
- [8] S. Cimino, L. Lisi, R. Pirone, G. Russo, Dual-site Pd/perovskite monolithic catalysts for methane catalytic combustion, *Ind. Eng. Chem. Res.* 43 (2004) 6670–6679.
- [9] Y. Wang, H. Arandiyani, J. Scott, M. Akia, H. Dai, J. Deng, K.-F. Aguey-Zinsou, R. Amal, High performance Au-Pd supported on 3D hybrid strontium-substituted lanthanum manganite perovskite catalyst for methane combustion, *ACS Catal.* 6 (2016) 6935–6947.
- [10] Y. Nishihata, J. Mizuki, T. Akao, H. Tanaka, M. Uenishi, M. Kimura, T. Okamoto, N. Hamadak, Self-regeneration of a Pd-perovskite catalyst for automotive emissions control, *Nature* 418 (2002) 164–167.
- [11] H. Tanaka, M. Taniguchi, M. Uenishi, N. Kajita, I. Tan, Y. Nishihata, J. Mizuki, K. Narita, M. Kimura, K. Kaneko, Self-regenerating Rh- and Pt-based perovskite catalysts for automotive-emissions control, *Angew. Chem. Int. Ed. Engl.* 45 (2006) 5998–6002.
- [12] J. Deng, M. Cai, W. Sun, X. Liao, W. Chu, X.S. Zhao, Oxidative methane reforming with an intelligent catalyst: sintering-tolerant supported nickel nanoparticles, *ChemSusChem* 6 (2013) 2061–2065.
- [13] P. Esmaeilnejad-Ahranjani, A.A. Khodadadi, Y. Mortazavi, Self-regenerative function of Cu in LaMnCu<sub>0.1</sub>O<sub>3</sub> catalyst: towards noble metal-free intelligent perovskites for automotive exhaust gas treatment, *Appl. Catal. A: Gen.* 602 (2020), 117702.
- [14] Z. Bao, V. Fung, F. Polo-Garzon, Z.D. Hood, S. Cao, M. Chi, L. Bai, D.-e Jiang, Z. Wu, The interplay between surface facet and reconstruction on isopropanol conversion over SrTiO<sub>3</sub> nanocrystals, *J. Catal.* 384 (2020) 49–60.
- [15] J. Zhang, Q. Daniel, T. Zhang, X. Wen, B. Xu, L. Sun, U. Bach, Y.B. Cheng, Chemical dopant engineering in hole recombination layers for efficient perovskite solar cells: insight into the interfacial recombination, *ACS Nano* 12 (2018) 10452–10462.
- [16] N. Phung, R. Felix, D. Meggiolaro, A. Al-Ashouri, E.S.G. Sousa, C. Hartmann, J. Hidalgo, H. Kobler, E. Mosconi, B. Lai, R. Gunder, M. Li, K.L. Wang, Z.K. Wang, K. Nie, E. Handick, R.G. Wilks, J.A. Marquez, B. Rech, T. Unold, J.P. Correa-Baena, S. Albrecht, F. De Angelis, M. Bar, A. Abate, The doping mechanism of halide perovskite unveiled by alkaline earth metals, *J. Am. Chem. Soc.* 142 (2020) 2364–2374.
- [17] B.H. Toby, R.B. Von Dreele, GSAS-II: the genesis of a modern open-source all purpose crystallography software package, *J. Appl. Crystallogr.* 46 (2013) 544–549.
- [18] Z. Wu, M. Li, J. Howe, H.M. Meyer III, S.H. Overbury, Probing defect sites on CeO<sub>2</sub> nanocrystals with well-defined surface planes by Raman spectroscopy and O<sub>2</sub> adsorption, *Langmuir* 26 (2010) 16595–16606.
- [19] G. Kresse, J. Furthmuller, Efficiency of ab-initio total energy calculations for metals and semiconductors using a plane-wave basis set, *Comput. Mater. Sci.* 6 (1996) 15–50.
- [20] G. Kresse, J. Furthmuller, Efficient iterative schemes for ab initio total-energy calculations using a plane-wave basis set, *Phys. Rev. B* 54 (1996) 11169–11186.
- [21] J.P. Perdew, K. Burke, M. Ernzerhof, Generalized gradient approximation made simple, *Phys. Rev. Lett.* 77 (1996) 3865–3868.
- [22] S. Grimme, J. Antony, S. Ehrlich, H. Krieg, A consistent and accurate ab initio parametrization of density functional dispersion correction (DFT-D) for the 94 elements H-Pu, *J. Chem. Phys.* 132 (2010), 154104.
- [23] P.E. Blöchl, Projector augmented-wave method, *Phys. Rev. B* 50 (1994) 17953–17979.
- [24] H.J. Monkhorst, J.D. Pack, Special points for brillouin-zone integrations, *Phys. Rev. B* 13 (1976) 5188–5192.
- [25] G. Henkelman, B.P. Uberuaga, H. Jónsson, A climbing image nudged elastic band method for finding saddle points and minimum energy paths, *J. Chem. Phys.* 113 (2000) 9901–9904.
- [26] V.V. Laguta, O.I. Scherbina, E.P. Garmash, V.N. Pavlikov, M.V. Karpe, M. D. Glinchuk, G.S. Svechnikov, Local structure and electron spin resonance of copper-doped SrTiO<sub>3</sub> ceramics, *J. Mater. Sci.* 48 (2013) 4016–4022.
- [27] T.K.-Y. Wong, B.J. Kennedy, C.J. Howard, B.A. Hunter, T. Vogt, Crystal structures and phase transitions in the SrTiO<sub>3</sub>-SrZrO<sub>3</sub> solid solution, *J. Solid State Chem.* 156 (2001) 255–263.
- [28] F. Polo-Garzon, S.Z. Yang, V. Fung, G.S. Foo, E.E. Bickel, M.F. Chisholm, D. E. Jiang, Z. Wu, Controlling reaction selectivity through the surface termination of perovskite catalysts, *Angew. Chem. Int. Ed. Engl.* 56 (2017) 9820–9824.
- [29] G.S. Foo, Z.D. Hood, Z. Wu, Shape effect undermined by surface reconstruction: ethanol dehydrogenation over shape-controlled SrTiO<sub>3</sub> nanocrystals, *ACS Catal.* 8 (2017) 555–565.
- [30] M. Rashad, M. Rüsing, G. Berth, K. Lischka, A. Pawlis, CuO and Co<sub>3</sub>O<sub>4</sub> nanoparticles: synthesis, characterizations, and Raman spectroscopy, *J. Nanomater.* 2013 (2013) 1–6.
- [31] J. Fang, Y. Xuan, Investigation of optical absorption and photothermal conversion characteristics of binary CuO/ZnO nanofluids, *RSC Adv.* 7 (2017) 56023–56033.
- [32] N. Mironova-Ulmane, A. Kuzmin, I. Sildos, M. Pärs, Polarisation dependent Raman study of single-crystal nickel oxide, *Open Phys.* 9 (2011).
- [33] M. Cuéllar-Cruz, D.K. Schneider, V. Stojanoff, S.R. Islas, N. Sánchez-Puig, R. Arreguin-Espinoza, J.M. Delgado, A. Moreno, Formation of crystalline silica-carbonate biomorphs of alkaline earth metals (Ca, Ba, Sr) from ambient to low temperatures: chemical implications during the primitive earth's life, *Cryst. Growth Des.* 20 (2019) 1186–1195.
- [34] I.A. Sluchinskaya, A.I. Lebedev, A. Erko, Structural position and oxidation state of nickel in SrTiO<sub>3</sub>, *J. Adv. Dielectr.* 03 (2013), 1350031.
- [35] P. Song, D. Wen, Z.X. Guo, T. Korakianitis, Oxidation investigation of nickel nanoparticles, *Phys. Chem. Chem. Phys.* 10 (2008) 5057–5065.
- [36] V. Vonk, N. Khorshidi, A. Stierle, Structure and oxidation behavior of nickel nanoparticles supported by YSZ(111), *J. Phys. Chem. C. Nanomater Interfaces* 121 (2017) 2798–2806.
- [37] J. Leitner, D. Sedmidubsky, M. Lojka, O. Jankovsky, The effect of nanosizing on the oxidation of partially oxidized copper nanoparticles, *Materials* 13 (2020).
- [38] A. Yabuki, S. Tanaka, Oxidation behavior of copper nanoparticles at low temperature, *Mater. Res. Bull.* 46 (2011) 2323–2327.
- [39] R. Auer, L. Warnier, F.C. Thyrian, Kinetic study of methane combustion over La<sub>0.9</sub>Ce<sub>0.1</sub>CoO<sub>3</sub>, in: G.F. Froment, K.C. Waugh (Eds.), *Studies in Surface Science and Catalysis*, Elsevier, 2001, pp. 599–604.
- [40] J. Chen, H. Arandiyani, X. Gao, J. Li, Recent advances in catalysts for methane combustion, *Catal. Surv. Asia* 19 (2015) 140–171.
- [41] Y. Wang, P. Hu, J. Yang, Y.A. Zhu, Chen, C-H bond activation in light alkanes: a theoretical perspective, *Chem. Soc. Rev.* 50 (2021) 4299–4358.